INSTITUT CLÉMENT ADER

Massively parallel methods for data-driven modelling and simulation in computational mechanics
Virtual workshop
September 23, 2020.

A fairly priced, unfitted spline image-based model to assist Digital Image Correlation

Ali Rouwane[1,2], Robin Bouclier[1,2], Jean-Charles Passieux[1] and Jean-Noël Périé[1]

rouwane@insa-toulouse.fr ; alirouwane@yahoo.com

1. Institut Clément Ader (ICA), Université de Toulouse, CNRS/INSA/Mines Albi/UPS/ISAE, Toulouse, France
2. Institut de Mathématiques de Toulouse (IMT), Université de Toulouse, CNRS/UT1/UT2/UT3/INSA, Toulouse, France

Introduction

Estimation of displacement and strain fields at the cellular scale of materials with complex cellular microstructures using Digital Image Correlation.

INSTITUT CLÉMENT ADER

Introduction

Estimation of displacement and strain fields at the cellular scale of materials with complex cellular microstructures using Digital Image Correlation.

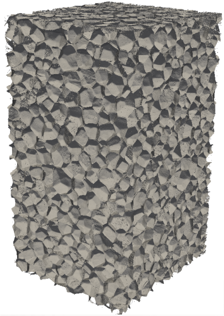

(a) Polymetacrylimid foam (Rohacell-51) image obtained from X-ray micro-tomography ✗

INSTITUT CLÉMENT ADER

Introduction

Estimation of displacement and strain fields at the cellular scale of materials with complex cellular microstructures using Digital Image Correlation.

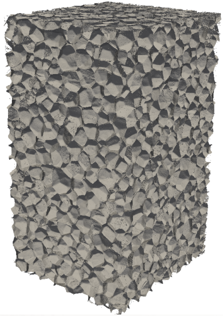

(a) Polymetacrylimid foam (Rohacell-51) image obtained from X-ray micro-tomography ✗

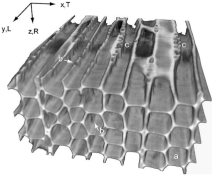

(b) Wood cell image obtained from X-ray micro-tomography Forsberg et al. [2008] ✗

Introduction

Estimation of displacement and strain fields at the cellular scale of materials with complex cellular microstructures using Digital Image Correlation.

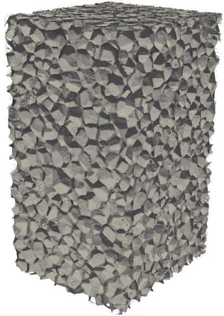

(a) Polymetacrylimid foam (Rohacell-51) image obtained from X-ray micro-tomography ✗

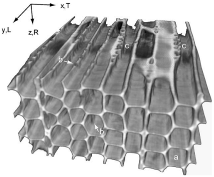

(b) Wood cell image obtained from X-ray micro-tomography Forsberg et al. [2008] ✗

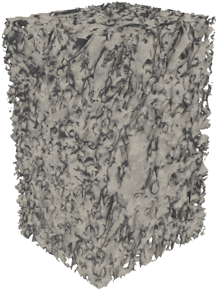

(c) Cattle bone image obtained from MRI Benoit et al. [2009] ✗

INSTITUT CLÉMENT ADER

Introduction

Estimation of displacement and strain fields at the cellular scale of materials with complex cellular microstructures using Digital Image Correlation.

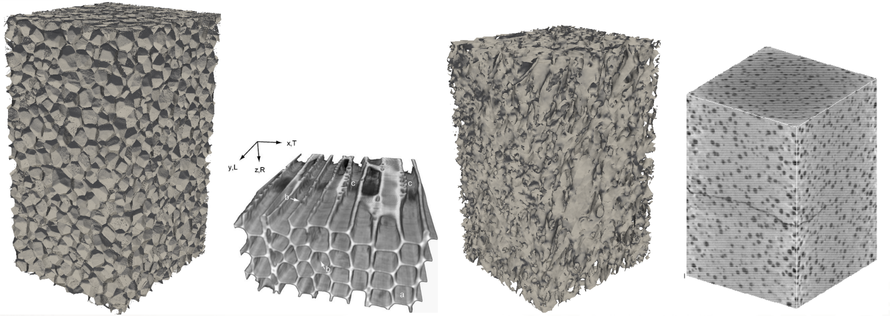

(a) Polymetacrylimid foam (Rohacell-51) image obtained from X-ray micro-tomography ✗

(b) Wood cell image obtained from X-ray micro-tomography Forsberg et al. [2008] ✗

(c) Cattle bone image obtained from MRI Benoit et al. [2009] ✗

(d) Nodular graphite cast iron image obtained from X-ray micro-tomography Limodin et al. [2009] ✔

Figure 1: Example of textures of complex materials.

More void than material ⟶ Poor texture makes the optimization problem difficult without using regularization schemes.

Contribution

- Develop a 2D DIC algorithm that allows to estimate the displacement behind transformation

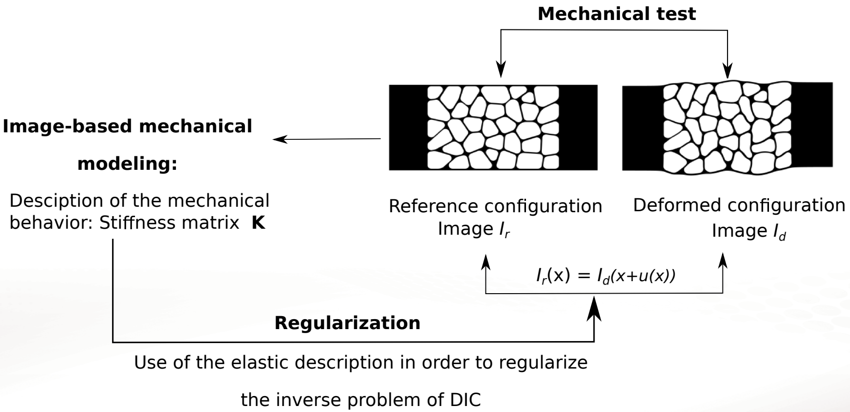

Figure 2: Summary of the methodology. Elastic regularization of DIC.

Outline

1. Building the stiffness operator **K** on the ROI using a fairly-priced image-based mechanical model

Outline

1. Building the stiffness operator **K** on the ROI using a fairly-priced image-based mechanical model
   - Recall of the FCM fictitious domain method

Outline

1. Building the stiffness operator **K** on the ROI using a fairly-priced image-based mechanical model
    - Recall of the FCM fictitious domain method
    - Presentation a geometry analysis study for fine-tuning the model's integration parameters

Outline

1. Building the stiffness operator **K** on the ROI using a fairly-priced image-based mechanical model
   - Recall of the FCM fictitious domain method
   - Presentation a geometry analysis study for fine-tuning the model's integration parameters
   - Presentation of a mechanical convergence study and confrontation with low order FEM image-based models.

Outline

1. Building the stiffness operator **K** on the ROI using a fairly-priced image-based mechanical model
    - Recall of the FCM fictitious domain method
    - Presentation a geometry analysis study for fine-tuning the model's integration parameters
    - Presentation of a mechanical convergence study and confrontation with low order FEM image-based models.
2. Use of the built stiffness operator for the regularization of Digital Image Correlation

B-splines as a numerical tool

- Deforming images by moving the control points of a B-spline control grid

(a) C^0 linear B-splines (same as linear lagrange functions)

(b) C^1 quadratic B-splines.

(c) C^2 cubic B-splines.

Figure 3: Image deformation with B-splines of $\mathcal{C}^{p-1}$ regularity at the element boundaries.

Construction of a fairly-priced image-based mechanical model with the Finite Cell Method

- Acquired image

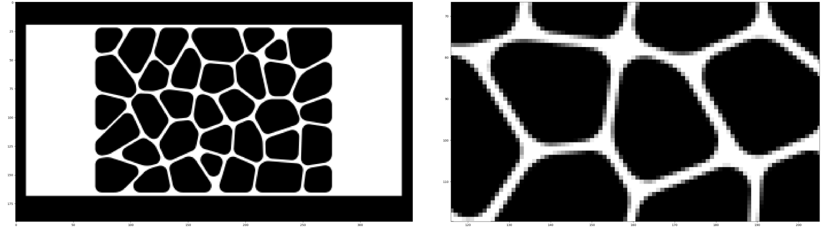

Figure 4: Image acquisition of a 2d sample with a complex geometry

Construction of a fairly-priced image-based mechanical model with the Finite Cell Method

- Level-set description of the geometry of two-phase materials:
  - Evolution level-sets based on the convection-diffusion equation Chan and Vese [2001]; Bernard et al. [2008]
  - Iso-value of a smooth physical representation of the target image Verhoosel et al. [2015]

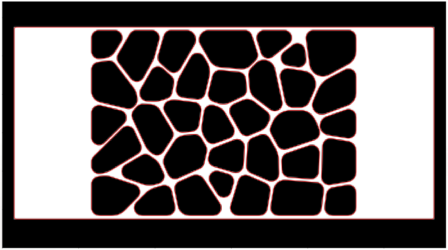

Construction of a fairly-priced image-based mechanical model with the Finite Cell Method

- Level-set description of the geometry of two-phase materials:
  - Evolution level-sets based on the convection-diffusion equation Chan and Vese [2001]; Bernard et al. [2008]
  - Iso-value of a smooth physical representation of the target image Verhoosel et al. [2015]

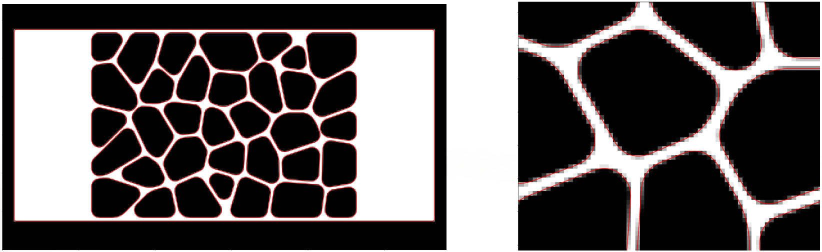

Figure 5: Level-set description of the physical domain.

Construction of a fairly-priced image-based mechanical model with the Finite Cell Method

- Embedding the image domain in a rectangular mesh Parvizian et al. [2007]; Schillinger and Ruess [2015]; Verhoosel et al. [2015]

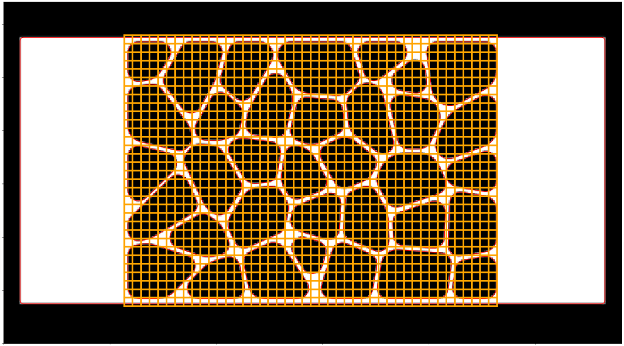

Figure 6: Embedding of the level-set geometry using a B-spline mesh (here the parametric space is equal to the physical space).

INSTITUT CLÉMENT ADER

Construction of a fairly-priced image-based mechanical model with the Finite Cell Method

- Integrating only on the physical domain. The level-set geometry is approximated by a quad-tree integration scheme Düster et al. [2008]; Schillinger and Ruess [2015] with a closure tesselation scheme Verhoosel et al. [2015].

Construction of a fairly-priced image-based mechanical model with the Finite Cell Method

- Integrating only on the physical domain. The level-set geometry is approximated by a quad-tree integration scheme Düster et al. [2008]; Schillinger and Ruess [2015] with a closure tesselation scheme Verhoosel et al. [2015].

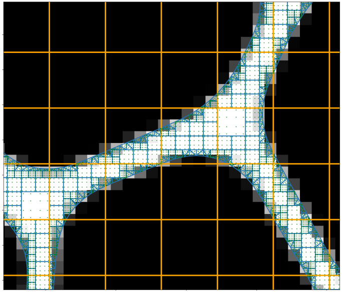

Figure 7: Image acquisition of an image of complex geometry

- Penalization of the stress tensor in the fictitious domain.

Construction of a fairly-priced image-based mechanical model with the Finite Cell Method

- Integrating only on the physical domain. The level-set geometry is approximated by a quad-tree integration scheme Düster et al. [2008]; Schillinger and Ruess [2015] with a closure tesselation scheme Verhoosel et al. [2015].

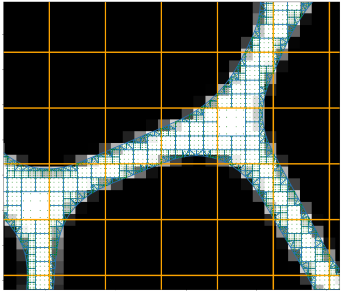

Figure 7: Image acquisition of an image of complex geometry

- Penalization of the stress tensor in the fictitious domain.
- Other closure integration techniques
  - Moment fitting methods Abedian et al. [2013]; Müller et al. [2013]; Joulaian et al. [2016]
  - Smart boundary conforming octrees Kudela et al. [2016]

Construction of a fairly-priced image-based mechanical model with the Finite Cell Method

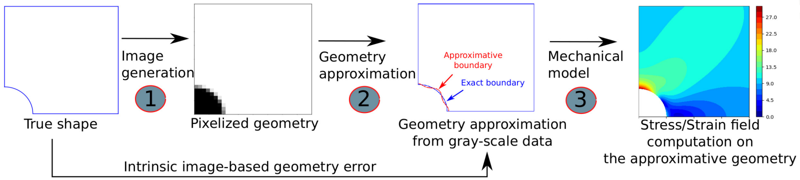

Figure 8: Summary of the different steps of the construction of a mechanical digital image-based model.

Construction of a fairly-priced image-based mechanical model with the Finite Cell Method

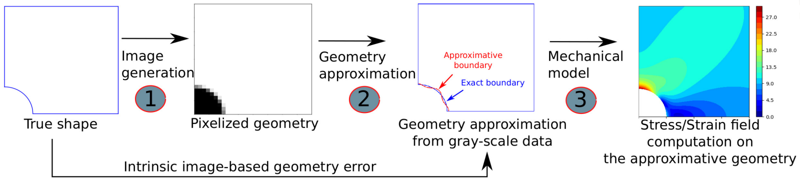

Figure 8: Summary of the different steps of the construction of a mechanical digital image-based model.

- Geometry error analysis

Construction of a fairly-priced image-based mechanical model with the Finite Cell Method

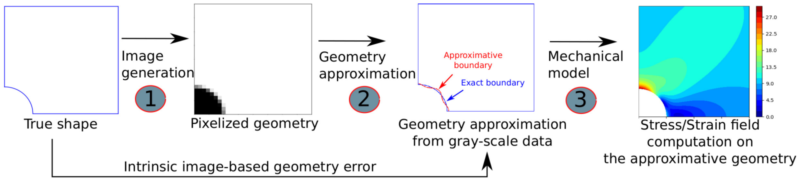

Figure 8: Summary of the different steps of the construction of a mechanical digital image-based model.

- Geometry error analysis
  - Intrinsic geometry error:

$$E = \frac{|\tilde{A} - A\,|}{A} \tag{1}$$

  - Total geometry error:

$$\bar{E} = \frac{|A_a - A|}{A} \tag{2}$$

  - Domain integration error:

$$\tilde{E} = \frac{|A_a - \tilde{A}|}{\tilde{A}} \tag{3}$$

where A_a is the approximation of the area bounded by the level-set using the quad-tree scheme. $\tilde{A}$ and A are respectively the area of the level-set geometry and the exact area of the reference geometry

- Geometric error evolution:

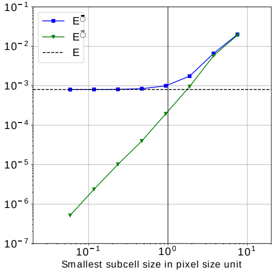

(a) 30 × 30 pixels in the image.

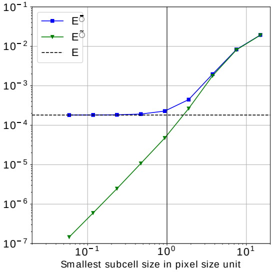

(b) 60 × 60 pixels in the image.

Figure 9: Evolution of the errors $\bar{E}$ and $\tilde{E}$ with respect to the size of the smallest sub-cell in pixel size units for the two-dimensional test case.

Construction of a fairly-priced image-based mechanical model with the Finite Cell Method

- Geometric error evolution:

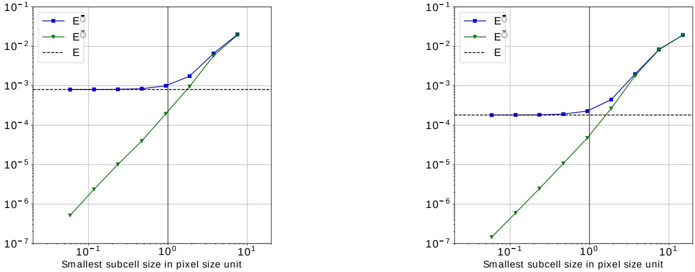

(a) 30 × 30 pixels in the image.

(b) 60 × 60 pixels in the image.

Figure 9: Evolution of the errors $\bar{E}$ and $\tilde{E}$ with respect to the size of the smallest sub-cell in pixel size units for the two-dimensional test case.

- A sufficient quad-tree level can be set so that the smallest sub-cell size is approximately equal to the pixel size.

$$l = \left\lceil \frac{1}{2} \log_2 \left(\frac{n_x n_y}{n_x^e n_y^e} \right) \right\rceil . \tag{4}$$

Comparison of the FCM image-based model to other Finite Element-based image models

We compare with three other lower finite element methods for computing the mechanical solution.

Comparison of the FCM image-based model to other Finite Element-based image models

We compare with three other lower finite element methods for computing the mechanical solution.

1.Voxel based model: Convert the connectivity of the binary image into a Q_4 finite element mesh Ulrich et al. [1998].

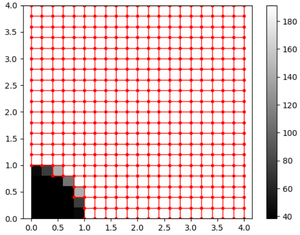

Figure 10: Finite element mesh of a binary image.

Comparison of the FCM image-based model to other Finite Element-based image models

We compare with three other lower finite element methods for computing the mechanical solution.

2.Marching squares algorithm: Extraction of a linear boundary and triangular meshing Lorensen and Cline [1987]; Frey et al. [1994]; Ulrich et al. [1998].

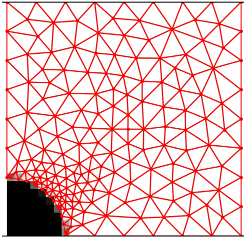

Figure 11: Extraction of a Finite element mesh using the marching squares algorithm.

Comparison of the FCM image-based model to other Finite Element-based image models

We compare with three other lower finite element methods for computing the mechanical solution.

3.Gray-level dependant mechanical properties : Assign each pixel a mechanical property that depends on its gray-level value. Example of a linear mechanical law for two materials.

$$E(v) = \frac{v - v_{min}}{v_{max} - v_{min}} E_{max} + \frac{v_{max} - v}{v_{max} - v_{min}} E_{min}$$

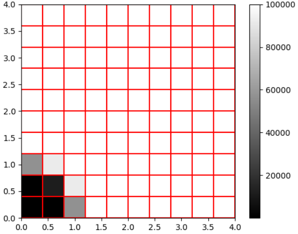

Figure 12: Mechanical propreties ranging from $1Pa$ to $10^5 Pa$.

Comparison of the FCM image-based model to other Finite Element-based image models

We compare with three other lower finite element methods for computing the mechanical solution.

4. Level-set based FCM with a triangular tesselation closure: Fictitious domain method on a linear triangular geometry approximating a continuous geometry defined by a level-set.

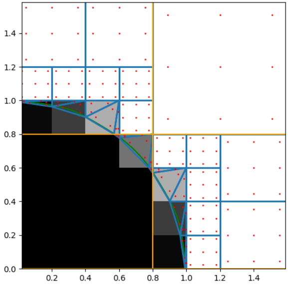

Figure 13: Fictitious domain method on a binary geometry.

Comparison of the FCM image-based model to other Finite Element-based image models

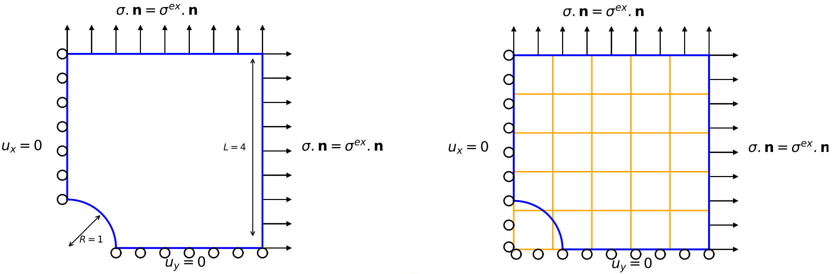

(a) Mechanical problem definition.

(b) An example of the embedding B-spline elements with the corresponding boundary conditions.

Figure 14: Mechanical problem definition: elastic plate with a quarter hole. The definition of σ^{ex} can be found in Sadd [2009]

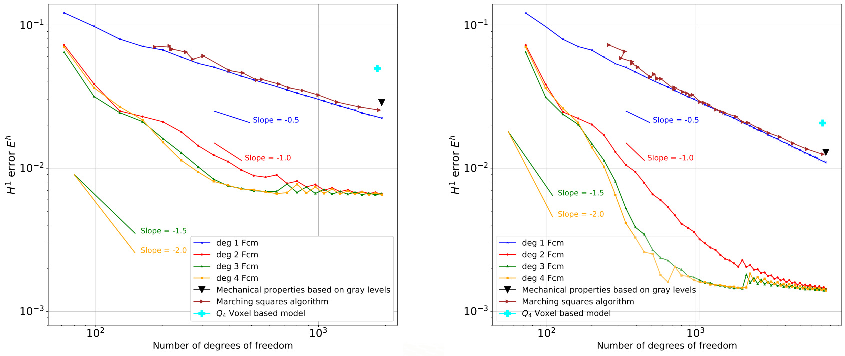

(a) 30 × 30 pixels in the image.

(b) 60 × 60 pixels in the image.

Figure 15: Evolution of the error in energy norm under mesh refinement.

INSTITUT CLÉMENT ADER

Digital Image Correlation for cellular images

The suggested methodology aims at estimating displacement fields at the cellular scale by solving the DIC problem:

$$I_r(x) = I_d(x + u(x)) \tag{5}$$

Digital Image Correlation for cellular images

The suggested methodology aims at estimating displacement fields at the cellular scale by solving the DIC problem:

$$I_r(x) = I_d(x + u(x)) \tag{5}$$

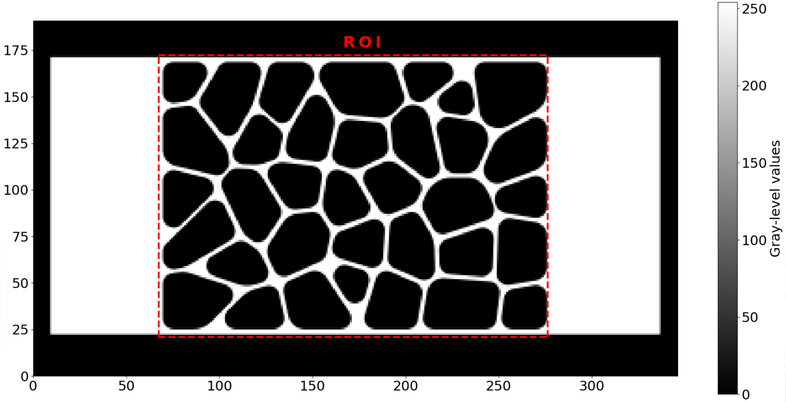

Figure 16: Image I_r

Digital Image Correlation for cellular images

The suggested methodology aims at estimating displacement fields at the cellular scale by solving the DIC problem:

$$I_r(x) = I_d(x + u(x)) \qquad (5)$$

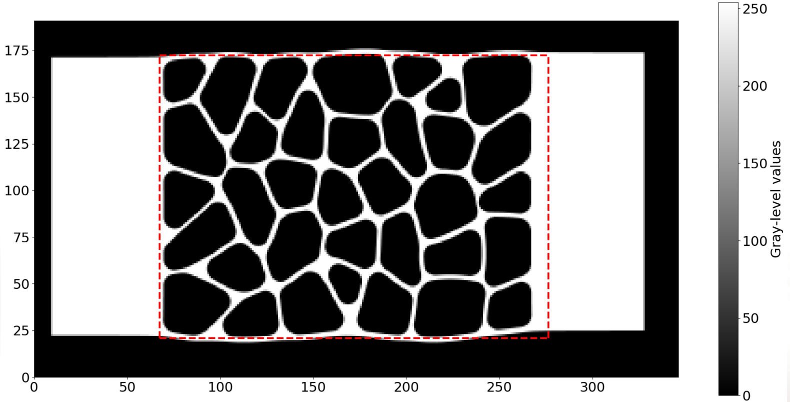

Figure 17: Image I_d

Digital Image Correlation for cellular images

- Displacement searched in a subspace of $L^2(\Omega)$ spanned by as set of basis functions:

$$u(x, y) = \mathbf{N}(x, y)\mathbf{u} \tag{6}$$

Digital Image Correlation for cellular images

- Displacement searched in a subspace of $L^2(\Omega)$ spanned by as set of basis functions:

$$u(x, y) = \mathbf{N}(x, y)\mathbf{u} \tag{6}$$

- Problem (5) is changed into the minimization of the squared L^2 norm

$$S(\mathbf{u}) = \frac{1}{2} \int_{\Omega} \left(I_r(x, y) - I_d((x, y) + \mathbf{N}(x, y)\mathbf{u}) \right)^2 dxdy \tag{7}$$

Digital Image Correlation for cellular images

- Multi-level displacement estimation using a Q_4 finite element mesh.

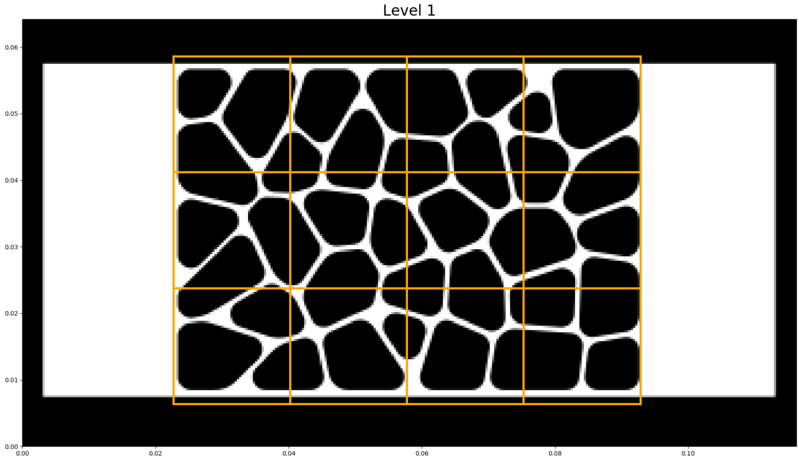

Figure 18: Level 1 of refinement

Digital Image Correlation for cellular images

- Multi-level displacement estimation using a Q_4 finite element mesh.

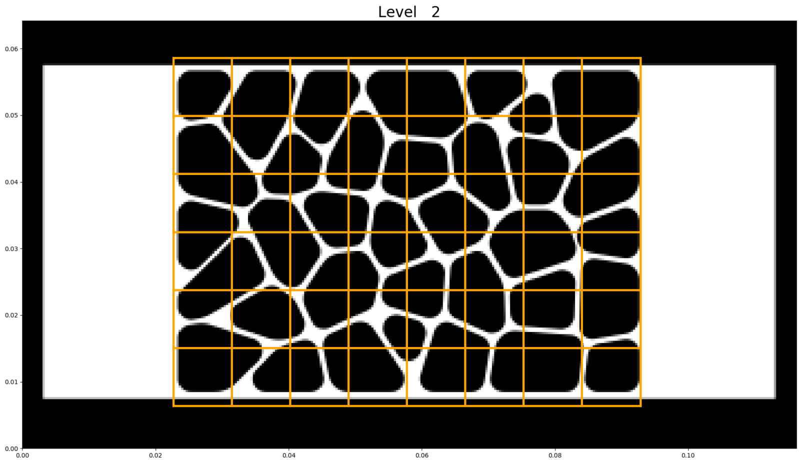

Figure 19: Level 2 of refinement

Digital Image Correlation for cellular images

- Multi-level displacement estimation using a Q_4 finite element mesh.

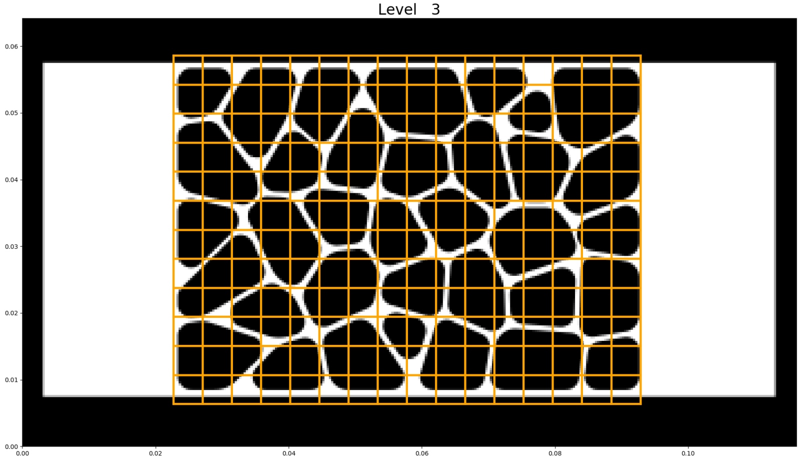

Figure 20: Level 3 of refinement

Digital Image Correlation for cellular images

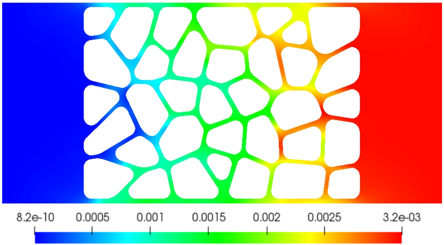

(a) Finite element reference displacement field.

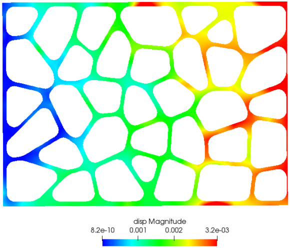

(b) Estimated displacemet field.

Figure 21: Displacement field comparison

Digital Image Correlation for cellular images

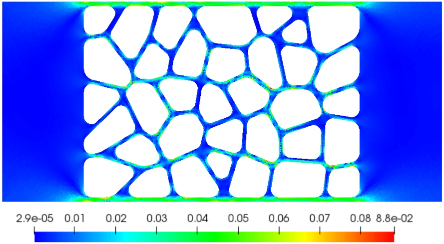

(a) Finite element reference displacement field.

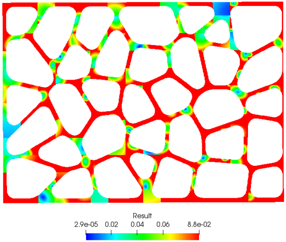

(b) Estimated displacemet field.

Figure 22: Strain field comparison

Image-based mechanical regularization of Digital Image Correlation

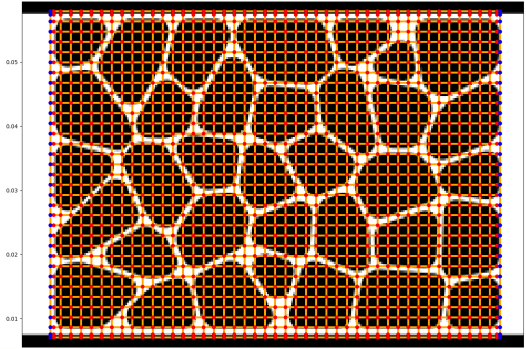

Figure 23: B-spline mesh displayed the grid of B-spline control points.

Image-based mechanical regularization of Digital Image Correlation

- Equilibrium gap regularization Réthoré et al. [2009]

$$M(\mathbf{u}) = \frac{1}{2}||\mathbf{K}\mathbf{u} - \mathbf{f}||_2^2$$

Image-based mechanical regularization of Digital Image Correlation

- Equilibrium gap regularization Réthoré et al. [2009]

$$M(\mathbf{u}) = \frac{1}{2}||\mathbf{Ku} - \mathbf{f}||_2^2 \quad \longrightarrow \quad M(\mathbf{u}) = \frac{1}{2}||\mathbf{D}_M\mathbf{Ku}||_2^2 \tag{8}$$

Image-based mechanical regularization of Digital Image Correlation

- Equilibrium gap regularization Réthoré et al. [2009]

$$M(\mathbf{u}) = \frac{1}{2}||\mathbf{Ku} - \mathbf{f}||_2^2 \quad \longrightarrow \quad M(\mathbf{u}) = \frac{1}{2}||\mathbf{D}_M\mathbf{Ku}||_2^2 \tag{8}$$

- First order gradient Tikhonov regularization

$$T(\mathbf{u}) = \frac{1}{2}||\mathbf{D}_T\mathbf{Lu}||_2^2 \tag{9}$$

Image-based mechanical regularization of Digital Image Correlation

- Equilibrium gap regularization Réthoré et al. [2009]

$$M(\mathbf{u}) = \frac{1}{2}||\mathbf{Ku} - \mathbf{f}||_2^2 \quad \longrightarrow \quad M(\mathbf{u}) = \frac{1}{2}||\mathbf{D}_M\mathbf{Ku}||_2^2 \tag{8}$$

- First order gradient Tikhonov regularization

$$T(\mathbf{u}) = \frac{1}{2}||\mathbf{D}_T\mathbf{Lu}||_2^2 \tag{9}$$

- The optimization functional

$$\arg\min_{\mathbf{u}\in\mathbb{R}^{2n}} \left[S(\mathbf{u}) + \lambda_M M(\mathbf{u}) + \lambda_T T(\mathbf{u})\right], \tag{10}$$

Image-based mechanical regularization of Digital Image Correlation

- Equilibrium gap regularization Réthoré et al. [2009]

$$M(\mathbf{u}) = \frac{1}{2}||\mathbf{Ku} - \mathbf{f}||_2^2 \quad \longrightarrow \quad M(\mathbf{u}) = \frac{1}{2}||\mathbf{D}_M\mathbf{Ku}||_2^2 \tag{8}$$

- First order gradient Tikhonov regularization

$$T(\mathbf{u}) = \frac{1}{2}||\mathbf{D}_T\mathbf{Lu}||_2^2 \tag{9}$$

- The optimization functional

$$\underset{\mathbf{u}\in\mathbb{R}^{2n}}{\arg\min} \left[S(\mathbf{u}) + \lambda_M M(\mathbf{u}) + \lambda_T T(\mathbf{u})\right], \tag{10}$$

- Problem (10) is solved with a modified Gauss-Newton scheme (see *e.g.* Passieux and Bouclier [2019] for more details on the optimization scheme).
  - Leads to an iterative scheme where a SPD linear system is solved at each iteration —> ill-conditionned Hessian due to the poor conditionning of the stiffness matrix

Numerical results: comparison of the euclidian norm of the displacement

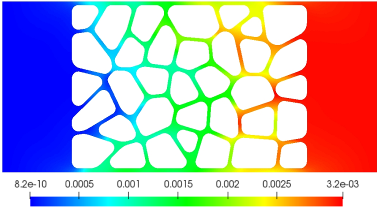

Reference finite element simulation

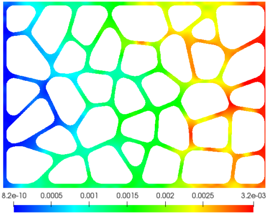

Tikhonov regularization

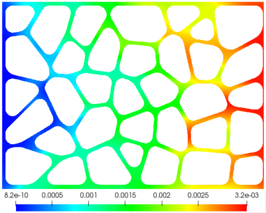

Equilibrium gap regularization

Numerical results: comparison of the Von-Mises strain norm of the displacement

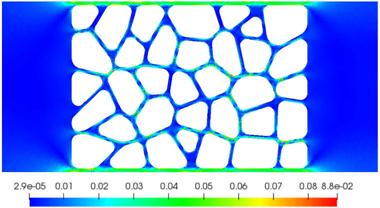

Reference finite element simulation

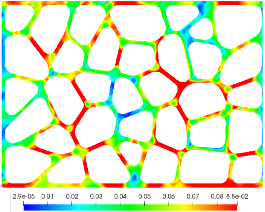

Tikhonov regularization

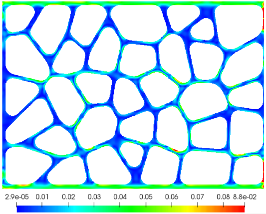

Equilibrium gap regularization

Numerical results: comparison of the Von-Mises strain norm of the displacement

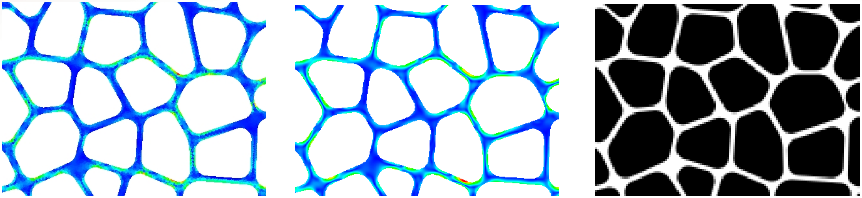

(a) Strain norm of the finite element simulation. (b) Strain norm of the registered solution. (c) Reference image I_r.

Figure 24: Zoom on a region in the ROI.

	$P(u_x)$ (pixels)	$P(u_y)$ (pixels)	$P(\varepsilon_{xx})$	$P(\varepsilon_{yy})$	$P(\varepsilon_{xy})$
Standard multi-level DIC	4.5×10^{-1}	1.9×10^{-1}	7.2×10^{-1}	1	4×10^{-1}
Tikhonov regularization	1.6×10^{-1}	1.1×10^{-1}	1.4	1.4	4.1×10^{-1}
Mechanical regularization	2×10^{-2}	3×10^{-2}	3.8×10^{-2}	1×10^{-2}	3.5×10^{-3}

Table 1: Precision of the measurements in terms of displacement and strain fields.

Conclusion and perspectives

- Conclusion
  - Fictitious domain methods (in particular the Finite Cell Method): an effective tool to image-based mechanical modeling
    - Setting of user defined parameters (Level-set parameters, quadrature rule, element size, order of approximation...)

Conclusion and perspectives

- Conclusion
  - Fictitious domain methods (in particular the Finite Cell Method): an effective tool to image-based mechanical modeling
    - Setting of user defined parameters (Level-set parameters, quadrature rule, element size, order of approximation...)
  - Digital imaging implies intrinsic geometry error due to pixelisation
    - The above user-defined parameters must be adapted to avoid over-computations.

Conclusion and perspectives

- Conclusion
  - Fictitious domain methods (in particular the Finite Cell Method): an effective tool to image-based mechanical modeling
    - Setting of user defined parameters (Level-set parameters, quadrature rule, element size, order of approximation...)
  - Digital imaging implies intrinsic geometry error due to pixelisation
    - The above user-defined parameters must be adapted to avoid over-computations.
  - We analysed these geometric and mechanical errors and proposed a pragmatic rule to set the Finite Cell Method parameters.
    - We end up with a so-called fairly priced image-based mechanical model which accuracy is the best possible with minimal numerical complexity.

Conclusion and perspectives

- Conclusion
  - Fictitious domain methods (in particular the Finite Cell Method): an effective tool to image-based mechanical modeling
    - Setting of user defined parameters (Level-set parameters, quadrature rule, element size, order of approximation...)
  - Digital imaging implies intrinsic geometry error due to pixelisation
    - The above user-defined parameters must be adapted to avoid over-computations.
  - We analysed these geometric and mechanical errors and proposed a pragmatic rule to set the Finite Cell Method parameters.
    - We end up with a so-called fairly priced image-based mechanical model which accuracy is the best possible with minimal numerical complexity.
- Perspectives
  - Generalization of the method to 3D and application to Digital Volume Correlation.
    - Until know direct sparse linear solvers are used (SuperLU)
    - Currently working on solving using other libraries (such as MUMPS)

Conclusion and perspectives

- Conclusion
  - Fictitious domain methods (in particular the Finite Cell Method): an effective tool to image-based mechanical modeling
    - Setting of user defined parameters (Level-set parameters, quadrature rule, element size, order of approximation...)
  - Digital imaging implies intrinsic geometry error due to pixelisation
    - The above user-defined parameters must be adapted to avoid over-computations.
  - We analysed these geometric and mechanical errors and proposed a pragmatic rule to set the Finite Cell Method parameters.
    - We end up with a so-called fairly priced image-based mechanical model which accuracy is the best possible with minimal numerical complexity.
- Perspectives
  - Generalization of the method to 3D and application to Digital Volume Correlation.
    - Until know direct sparse linear solvers are used (SuperLU)
    - Currently working on solving using other libraries (such as MUMPS)
  - Application with real *in-situ* mechanical tests using computed Micro-tomography.

Bibliography I

Abedian, A., Parvizian, J., Düster, A., Khademyzadeh, H., and Rank, E. (2013). Performance of different integration schemes in facing discontinuities in the finite cell method. *International Journal of Computational Methods*, 10(03):1350002.

Benoit, A., Guérard, S., Gillet, B., Guillot, G., Hild, F., Mitton, D., Périé, J.-N., and Roux, S. (2009). 3d analysis from micro-mri during in situ compression on cancellous bone. *Journal of Biomechanics*, 42(14):2381 – 2386.

Bernard, O., Friboulet, D., Thevenaz, P., and Unser, M. (2008). Variational b-spline level-set method for fast image segmentation. In *2008 5th IEEE International Symposium on Biomedical Imaging: From Nano to Macro*, pages 177–180.

Chan, T. F. and Vese, L. A. (2001). Active contours without edges. *IEEE Transactions on Image Processing*, 10(2):266–277.

Düster, A., Parvizian, J., Yang, Z., and Rank, E. (2008). The finite cell method for three-dimensional problems of solid mechanics. *Computer methods in applied mechanics and engineering*, 197(45-48):3768–3782.

Forsberg, F., Mooser, R., Arnold, M., Hack, E., and Wyss, P. (2008). 3d micro-scale deformations of wood in bending: Synchrotron radiation μct data analyzed with digital volume correlation. *Journal of Structural Biology*, 164(3):255 – 262.

Frey, P., Sarter, B., and Gautherie, M. (1994). Fully automatic mesh generation for 3-d domains based upon voxel sets. *International Journal for Numerical Methods in Engineering*, 37(16):2735–2753.

Bibliography II

Joulaian, M., Hubrich, S., and Düster, A. (2016). Numerical integration of discontinuities on arbitrary domains based on moment fitting. *Computational Mechanics*, 57(6):979–999.

Kudela, L., Zander, N., Kollmannsberger, S., and Rank, E. (2016). Smart octrees: Accurately integrating discontinuous functions in 3d. *Computer Methods in Applied Mechanics and Engineering*, 306:406 – 426.

Limodin, N., Réthoré, J., Buffière, J.-Y., Gravouil, A., Hild, F., and Roux, S. (2009). Crack closure and stress intensity factor measurements in nodular graphite cast iron using three-dimensional correlation of laboratory x-ray microtomography images. *Acta materialia*, 57(14):4090–4101.

Lorensen, W. E. and Cline, H. E. (1987). Marching cubes: A high resolution 3d surface construction algorithm. *Computer Graphics*, 21(4):163–169.

Müller, B., Kummer, F., and Oberlack, M. (2013). Highly accurate surface and volume integration on implicit domains by means of moment-fitting. *International Journal for Numerical Methods in Engineering*, 96(8):512–528.

Parvizian, J., Düster, A., and Rank, E. (2007). Finite cell method. *Computational Mechanics*, 41(1):121–133.

Passieux, J.-C. and Bouclier, R. (2019). Classic and inverse compositional gauss-newton in global dic. *International Journal for Numerical Methods in Engineering*.

Bibliography III

Réthoré, J., Roux, S., and Hild, F. (2009). An extended and integrated digital image correlation technique applied to the analysis of fractured samples. *European Journal of Computational Mechanics*, 18(3-4):285–306.

Sadd, M. H. (2009). *Elasticity: theory, applications, and numerics*. Academic Press.

Schillinger, D. and Ruess, M. (2015). The finite cell method: A review in the context of higher-order structural analysis of cad and image-based geometric models. *Archives of Computational Methods in Engineering*, 22(3):391–455.

Ulrich, D., van Rietbergen, B., Weinans, H., and Rüegsegger, P. (1998). Finite element analysis of trabecular bone structure: a comparison of image-based meshing techniques. *Journal of Biomechanics*, 31(12):1187 – 1192.

Verhoosel, C., van Zwieten, G., van Rietbergen, B., and de Borst, R. (2015). Image-based goal-oriented adaptive isogeometric analysis with application to the micro-mechanical modeling of trabecular bone. *Computer Methods in Applied Mechanics and Engineering*, 284:138 – 164. Isogeometric Analysis Special Issue.

Penalization of mechanical properties for the FCM method

The constitutive behavior law is modified by considering the penalized stress tensor defined by:

$$\sigma_\alpha(x, y) = \alpha(x, y)\sigma, \tag{11}$$

with

$$\alpha(x, y) = \begin{cases} \alpha_p = 1 \quad \forall (x, y) \in \Omega_p \\ \alpha_f = 10^{-q} << 1 \quad \forall (x, y) \in \Omega_f \end{cases} . \tag{12}$$

Instead of performing $\mathbf{K}_{\Omega_f}(\alpha_f) + \mathbf{K}_{\Omega_p}(\alpha_p)$ we assemble two stiffness matrices (one homogeneous on all elements) and one only on the integration domain

$$\mathbf{K} = \mathbf{K}_{\Omega}(\alpha_f) + \mathbf{K}_{\Omega_p}(\alpha_p - \alpha_f). \tag{13}$$

Optimization scheme

The resolution of the regularized non-linear least squares problem (10) is performed using the following descent scheme:

$$\mathbf{u}^{(k+1)} = \mathbf{u}^{(k)} + \mathbf{d}^{(k)}, \tag{14}$$

where $\mathbf{d}^{(k)}$ is the solution of the following Gauss-Newton system:

$$\left(\mathbf{H}_S(\mathbf{u}^{(k)}) + \lambda_M \mathbf{H}_M(\mathbf{u}^{(k)}) + \lambda_T \mathbf{H}_T(\mathbf{u}^{(k)})\right) \mathbf{d}^{(k)} = -\left(\nabla S(\mathbf{u}^{(k)}) + \lambda_M \nabla M(\mathbf{u}^{(k)}) + \lambda_T \nabla T(\mathbf{u}^{(k)})\right) \tag{15}$$

and where $\mathbf{H}_S$ is an approximation using only first-order derivatives of the Hessian matrix of S. $\mathbf{H}_M$ and $\mathbf{H}_T$ are respectively the Hessian matrices of M and T and $\nabla_S, \nabla_M, \nabla_T$ are respectively the gradient vectors of S, M and T. The definition of theses six operators is given by equations (16), (17), (18) and (19), see below:

$$\nabla S(\mathbf{u}^{(k)}) = -\int_\Omega \left(I_r(x,y) - I_d\left((x,y) + \mathbf{N}(x,y)\mathbf{u}^{(k)}\right)\right) \mathbf{N}(x,y)^T \nabla \mathbf{I_r}(x,y)dxdy; \tag{16}$$

$$\nabla M(\mathbf{u}^{(k)}) = \mathbf{K}^T \mathbf{D}_M^T \mathbf{D}_M \mathbf{K}\mathbf{u}^{(k)}, \quad \nabla T(\mathbf{u}^{(k)}) = \mathbf{L}^T \mathbf{D}_T^T \mathbf{D}_T \mathbf{L}\mathbf{u}^{(k)}; \tag{17}$$

$$\mathbf{H}_S(\mathbf{u}^{(k)}) = \int_\Omega \mathbf{N}(x,y)^T (\nabla \mathbf{I_d}) \left((x,y) + \mathbf{N}(x,y)\mathbf{u}^{(k)}\right)^T (\nabla \mathbf{I_d}) \left((x,y) + \mathbf{N}(x,y)\mathbf{u}^{(k)}\right) \mathbf{N}(x,y)dxdy; \tag{18}$$

$$\mathbf{H}_M = \mathbf{K}^T \mathbf{D}_M^T \mathbf{D}_M \mathbf{K}, \quad \mathbf{H}_T = \mathbf{L}^T \mathbf{D}_T^T \mathbf{D}_T \mathbf{L}. \tag{19}$$

Optimization scheme

$$\mathcal{T}(u) = \frac{1}{2}\int_\Omega \|\nabla u_x\|_2^2 + \|\nabla u_y\|_2^2 dxdy = \int_\Omega \left(\frac{\partial u_x}{\partial x}\right)^2 + \left(\frac{\partial u_x}{\partial y}\right)^2 + \left(\frac{\partial u_y}{\partial x}\right)^2 + \left(\frac{\partial u_y}{\partial y}\right)^2 dxdy. \quad (20)$$

The discrete form directly coming from $\mathcal{T}$ is given by:

$$\tilde{T}(\mathbf{u}) = \frac{1}{2}\int_\Omega \sum_{i=1}^{4} ||\mathbf{L}_i(x,y)\mathbf{u}||^2 dxdy = \frac{1}{2}\mathbf{u}^T \left(\int_\Omega \sum_{i=1}^{4} \mathbf{L}_i^T(x,y)\mathbf{L}_i(x,y)dxdy\right)\mathbf{u} = \frac{1}{2}\mathbf{u}^T\mathbf{L}\mathbf{u}, \quad (21)$$

where $\mathbf{L_i}$ are first order partial differential operators. $\mathbf{L}$ is called the Tikhonov linear operator. In order to properly select the DOF where the Tikhonov regularization will be applied, we will eventually consider a slightly different discrete cost function, based on the euclidean norm of the action of the Tikhonov operator instead of the scalar product:

$$\tilde{T}(\mathbf{u}) = \frac{1}{2}||\mathbf{L}\mathbf{u}||_2^2. \quad (22)$$